Noninvasive Optical Imaging of Nanomedicine Biodistribution

Sijumon Kunjachan,[†,∥] Felix Gremse,[†,∥] Benjamin Theek,[†] Patrick Koczera,[†] Robert Pola,[‡] Michal Pechar,[‡] Tomas Etrych,[‡] Karel Ulbrich,[‡] Gert Storm,[§,⊥] Fabian Kiessling,[†,*] and Twan Lammers[†,§,⊥,*]

[†]Department of Experimental Molecular Imaging, Helmholtz Institute for Biomedical Engineering, RWTH-Aachen University, Aachen, Germany, [‡]Institute of Macromolecular Chemistry, Academy of Sciences of the Czech Republic, Prague, Czech Republic, [§]Department of Targeted Therapeutics, MIRA Institute for Biomedical Technology and Technical Medicine, University of Twente, Enschede, The Netherlands, and [⊥]Department of Pharmaceutics, Utrecht Institute for Pharmaceutical Sciences, Utrecht University, Utrecht, The Netherlands. [∥]These authors contributed equally to this work.

ABSTRACT Nanomedicines are sub-micrometer-sized carrier materials designed to improve the biodistribution of i.v. administered (chemo-) therapeutic agents. In recent years, ever more efforts in the nanomedicine field have employed optical imaging (OI) techniques to monitor biodistribution and target site accumulation. Thus far, however, the longitudinal assessment of nanomedicine biodistribution using OI has been impossible, due to limited light penetration (in the case of 2D fluorescence reflectance imaging; FRI) and to the inability to accurately allocate fluorescent signals to nonsuperficial organs (in the case of 3D fluorescence molecular tomography; FMT). Using a combination of high-resolution microcomputed tomography (μCT) and FMT, we have here set out to establish a hybrid imaging protocol for noninvasively visualizing and quantifying the accumulation of near-infrared fluorophore-labeled nanomedicines in tissues other than superficial tumors. To this end, HPMA-based polymeric drug carriers were labeled with Dy750, their biodistribution and tumor accumulation were analyzed using FMT, and the resulting data sets were fused with anatomical μCT data sets in which several different physiologically relevant organs were presegmented. The robustness of 3D organ segmentation was validated, and the results obtained using 3D CT-FMT were compared to those obtained upon standard 3D FMT and 2D FRI. Our findings convincingly demonstrate that combining anatomical μCT with molecular FMT facilitates the noninvasive assessment of nanomedicine biodistribution.

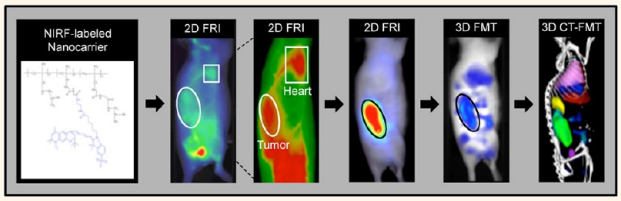

KEYWORDS: nanomedicine · drug targeting · biodistribution · FMT · FRI · CT

Nanomedicines aim to deliver drugs and imaging agents more efficiently and more specifically to pathological sites. A significant amount of evidence has been obtained over the years exemplifying the superiority of nanomedicine formulations over free drugs, both at the preclinical and at the clinical level.[1−5] Prototypic examples of nanomedicine formulations are liposomes, polymers, micelles, and nanoparticles. These sub-micrometer-sized carrier materials are designed to modulate the pharmacokinetics and the biodistribution of conjugated or entrapped (chemo-) therapeutic drugs. Upon intravenous (i.v.) administration, the prolonged circulation times of nanomedicines generally lead to passive accumulation in tumors or at sites of inflammation *via* the enhanced permeability and retention (EPR) effect.[6−8] At the same time, their nanosize prevents them from accumulating in (the vast majority of) healthy organs and tissues. Consequently, by increasing drug levels at pathological sites and reducing their concentrations in potentially endangered healthy tissues, nanomedicine formulations are able to improve the balance between the efficacy and the toxicity of systemic (chemo-) therapeutic interventions.[9−13]

To better understand and (further) improve nanomedicine-mediated drug targeting, it is important to quantitatively assess their biodistribution, their target site localization, and their accumulation in healthy organs and tissues. This can be done either invasively, by taking blood, tumor, and tissue samples at several different time points after i.v. administration or noninvasively, using various different imaging techniques. Examples of noninvasive imaging modalities routinely used for monitoring the biodistribution and the target site accumulation of nanomedicine formulations are positron emission tomography (PET), single photon emission

* Address correspondence to fkiessling@ukaachen.de, tlammers@ukaachen.de.

Received for review August 28, 2012 and accepted October 15, 2012.

Published online October 15, 2012
10.1021/nn303955n

computed tomography (SPECT), magnetic resonance imaging (MRI), and optical imaging (OI).[14,15] Among these, OI is the most recently established imaging modality for noninvasively visualizing nanomedicines *in vivo*. Because of its time- and cost-effectiveness, its user-friendliness, and its ability to be used for high-throughput analyses, OI has become extremely popular in recent years, and it is about to surpass nuclear medicine- and MR-based imaging techniques in the drug delivery field.

The vast majority of OI systems and strategies currently used in nanomedicine research are based on planar 2D fluorescence reflectance imaging (FRI).[16−25] FRI is generally considered to be an excellent tool for monitoring nanomedicine accumulation in superficial tissues, such as subcutaneously inoculated tumors, but it is unable to provide quantitative information, and it also does not allow for the assessment of nanomedicine accumulation in deeper-seated tissues.[26] This means that it can be used for qualitative and comparative analyses, in which the kinetics of EPR-mediated passive drug targeting to tumors are being visualized or in which the tumor accumulation of several different nanomedicine formulations is being compared. FRI is unsuitable, however, for analyzing absolute amounts accumulating in the tumors, as well as for noninvasively assessing nanomedicine accumulation in physiologically relevant healthy organs.

Fluorescence molecular tomography (FMT), on the other hand, in which lasers are used to excite near-infrared fluorophores (NIRF) in small laboratory animals at up to 120 spatial locations, for which planar detectors such as CCD cameras record excitation and emission images of the diffuse light propagation, and in which advanced algorithms volumetrically reconstruct the accumulation in and the concentration of optical imaging agents, is generally considered to be able to overcome some of the shortcomings associated with OI and to enable more quantitative and more in-depth analyses of NIRF-labeled (nano-) materials in nonsuperficial tissues. The major shortcoming of FMT, however, relates to its inability to accurately assign the reconstructed probe accumulation signal to a given organ of interest.[27−30] This likely is the main reason why 3D FMT has thus far not yet been used to noninvasively and quantitatively assess the whole-body biodistribution of NIRF-labeled nanomedicine formulations.

Extending several pioneering efforts with regard to the combination of FMT with microcomputed tomography (μCT) for molecular imaging purposes,[31−33] using *N*-(2-hydroxypropyl)methacrylamide (HPMA)-based and NIRF-labeled polymeric nanocarriers known to accumulate in tumors both effectively and selectively by means of EPR,[10,12,34,35] we here show that hybrid CT-FMT imaging can be employed to noninvasively assess the accumulation of nanomedicine formulations in tissues other than superficial/subcutaneous tumors. To this end, the biodistribution and tumor accumulation of 5−10 nm sized Dy750-labeled polymeric carrier materials were visualized and quantified using 3D FMT, and the data sets obtained were fused with 3D anatomical μCT data sets in which several different physiologically relevant organs were presegmented. The robustness of 3D organ segmentation and probe accumulation was validated by comparing and correlating the results of two independent observers. Furthermore, the biodistributional patterns obtained upon 3D *in vivo* CT-FMT were compared to those obtained using standard 3D *in vivo* FMT, as well as to those obtained upon 2D *in vivo* and *ex vivo* FRI, together convincingly demonstrating that although several conceptual shortcomings with regard to *in vivo* optical imaging still need to be overcome, combining μCT with FMT enables the noninvasive assessment of nanomedicine biodistribution.

RESULTS AND DISCUSSION

Monitoring the Biodistribution of pHPMA-Dy750 Using 2D FRI and 3D FMT. The chemical structure of a Dy750-labeled polymeric drug carrier is shown in Figure 1. The molecular weight of this conjugate was 67 kDa, and its polydispersity was 1.7. Upon i.v. injection, its biodistribution was initially investigated using 2D FRI and 3D FMT. Representative images are provided in Figure 2. At the early time points after i.v. injection, that is, up to 1 h after administration, 2D FRI qualitatively confirmed the long-circulating properties of the copolymer, showing localization in heart and in large blood vessels (upper two panels in Figure 2A). In addition, a relatively strong accumulation in the urinary bladder was observed, indicating kidney clearance (note that animals were under continuous anesthesia during the first hour, leading to progressive probe accumulation in the bladder). Also, the 3D FMT images obtained at these early time points confirmed the long-circulating properties of pHPMA-Dy750 (compare the squares in the middle panels in Figure 2A with similar regions in the lower panels in Figure 2A). Importantly, however, they did not allow for a meaningful interpretation of probe accumulation in tumors and in healthy organs. At later time points, as exemplified by Figure 2B, pHPMA-Dy750 efficiently accumulated in tumors by means of EPR. Both 2D FRI and 3D FMT indicated significant probe accumulation in tumors. Both, however, turned out to be unable to provide representative information with regard to the accumulation of pHPMA-Dy750 in healthy nontarget tissues.

In line with the literature,[21−31] comparing 2D FRI to 3D FMT showed that the latter more realistically reflected the biodistribution of pHPMA-Dy750 than the former (which essentially only indicated highly effective and highly selective probe accumulation in tumors; see upper panels in Figure 2B). When we take into account previous results obtained with regard to the biodistribution of radiolabeled HPMA-based polymeric drug carriers,[12,34,36−39] however, 3D FMT

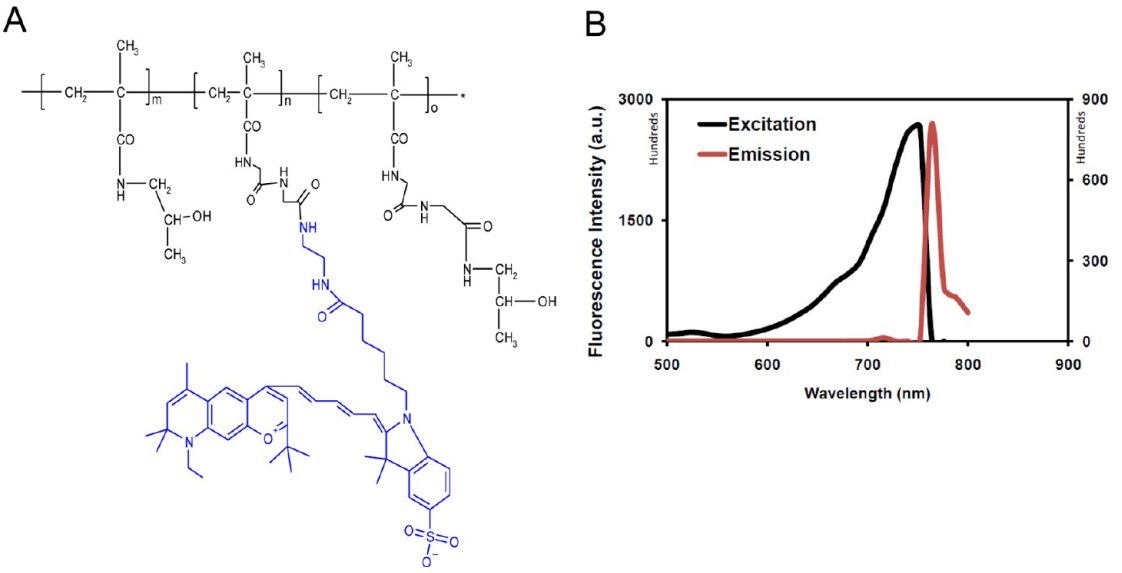

Figure 1. (A) Chemical structure of pHPMA-Dy750. (B) Spectrophotometric analysis of pHPMA-Dy750 excitation and emission.

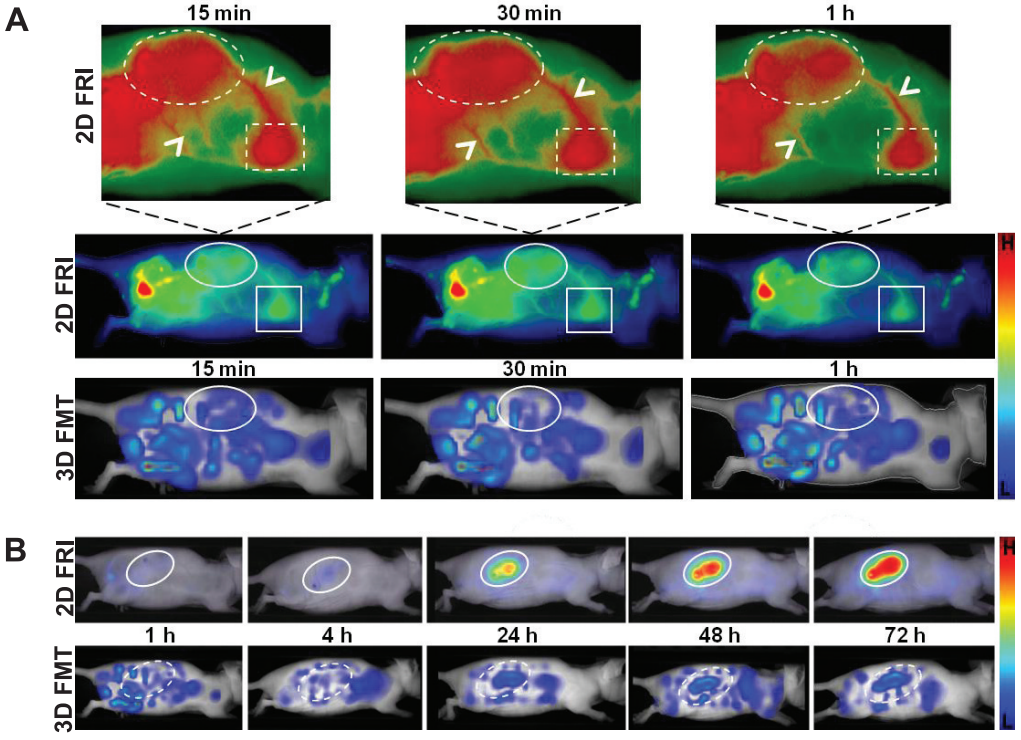

Figure 2. Optical imaging of pHPMA-Dy750 biodistribution using 2D FRI and 3D FMT. (A) As shown in the top panels, at the early time points after i.v. administration, 2D FRI was found to be suitable for monitoring the long-circulating properties of pHPMA-Dy750, as exemplified by strong signals in heart (squares) and in large blood vessels (arrows). The middle and bottom panels exemplify that, at these early time points, also already some accumulation in tumors (circles) could be observed in CT26 colon carcinoma-bearing nude mice. (B) At later time points, progressive EPR-mediated tumor accumulation could be observed, using both 2D FRI (top panels) and 3D FMT (bottom panels). In addition, the images convincingly show that no meaningful information on pHPMA-Dy750 accumulation in healthy nontarget tissues could be obtained, neither using 2D FRI nor using 3D FMT (because anatomical organ boundaries cannot be delineated).

also did not properly reflect tumor and healthy organ accumulation. As exemplified by the lower panels in Figure 2B, apart from significant accumulation in tumors and some residual signal that could be allocated to the heart (*i.e.*, to prolonged circulation), a relatively punctuate pattern of probe accumulation was observed within the abdomen of the mice, especially at 48 h (see lower panel in Figure 2B), which does not comply with the pharmacokinetic properties and with the physiological distribution of this carrier construct at

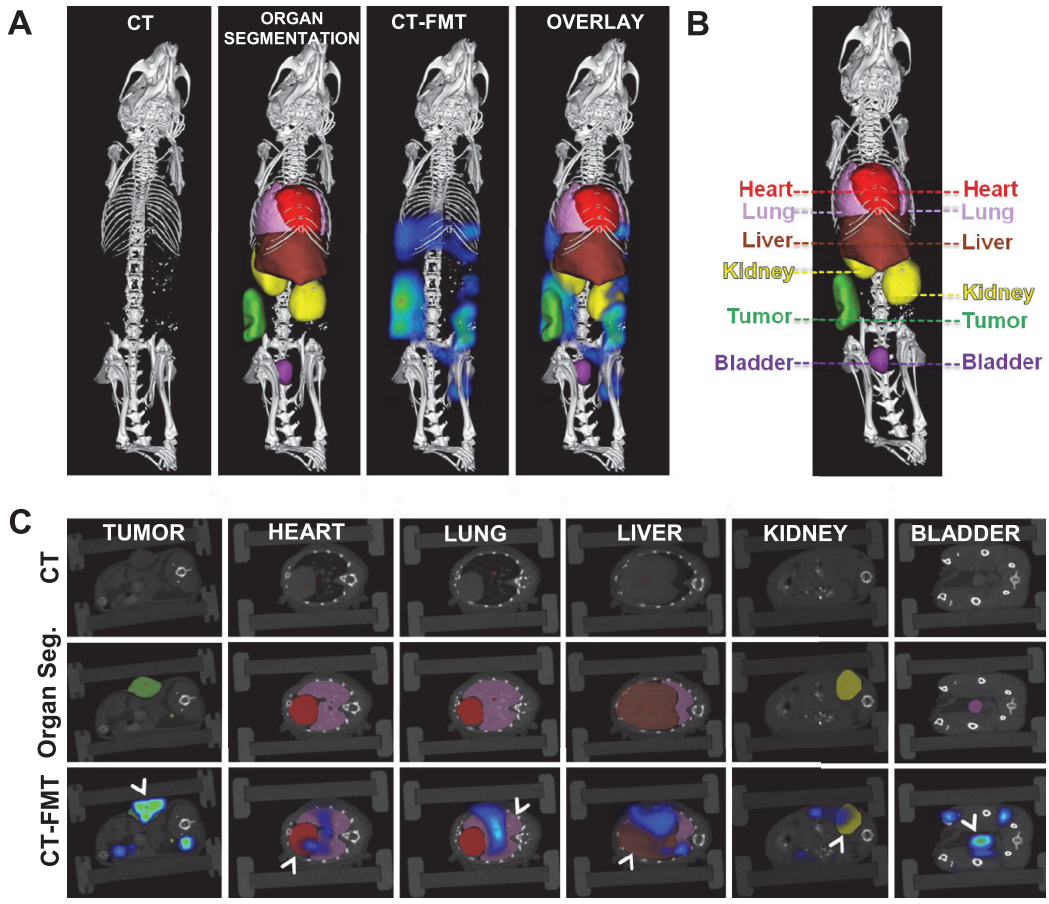

Figure 3. CT-based organ segmentation and hybrid CT-FMT imaging. (A) High-resolution μCT scans of CT26 colon carcinoma-bearing nude mice, depicting highly electron-dense anatomical structures (*i.e.*, bones), presegmented organs (cf. panel C), FMT-based biodistribution data overlaid on highly electron-dense anatomical structures, and FMT-based biodistribution data overlaid on presegmented organs. (B,C) Two-dimensional planes representing individual organs (B) and pHPMA-Dy750 accumulation in (cross sections of) these organs (C), analyzed upon fusing μCT and FMT data sets.

this time point. These findings therefore convincingly demonstrate that both 2D FRI and 3D FMT are useful for qualitatively monitoring the accumulation of nanomedicine formulations in superficial (subcutaneous) tumors but not for providing a meaningful interpretation and a realistic real-time reflection of their biodistribution and their accumulation in nontarget tissues.

CT-Based Organ Segmentation and Hybrid CT-FMT Imaging. To overcome this shortcoming with regard to noninvasively assessing nanomedicine biodistribution using OI, we have set out to develop a hybrid CT-FMT protocol, based on 3D organ segmentation using μCT and on the subsequent fusion of the μCT data sets with 3D FMT information on the biodistribution of pHPMA-Dy750. This protocol is exemplified in Figure 3A. First, prior to the biodistribution of the NIRF-labeled nanocarrier formulation being monitored, μCT imaging is performed, and on the basis of this, several different physiologically relevant organs are manually presegmented. The left panel in Figure 3A shows a CT image of a mouse windowed in such a way that highly dense (bone) anatomical structures are displayed. By altering the windowing protocol, that is, by also including somewhat less electron-dense signals, several different organs can be presegmented relatively easily using non-contrast-enhanced CT, enabling the discrimination and identification of tumor, heart, liver, lung, kidney- and bladder (NB: for identifying additional physiologically relevant organs, such as spleen, contrast-enhanced μCT has to be employed). This is visually exemplified in the top panels in Figure 3C, which very clearly show the density difference between heart and lung. On the basis of such μCT images, 3D volumes could be allocated to respective organs (second panel in Figure 3A), and upon this information being fused with the data sets obtained using 3D FMT (third panel in Figure 3A), CT-FMT overlays were obtained (right panel in Figure 3A), enabling a much more accurate analysis of nanomedicine accumulation in nonsuperficial tissues. The 2D planes of organs presegmented are shown in Figure 3B, and the corresponding 2D overlays of μCT and FMT are provided in Figure 3C. Using such setups, 3D organ volumes could be determined, and the accumulation of pHPMA-Dy750 in these organs could be visualized and quantified.

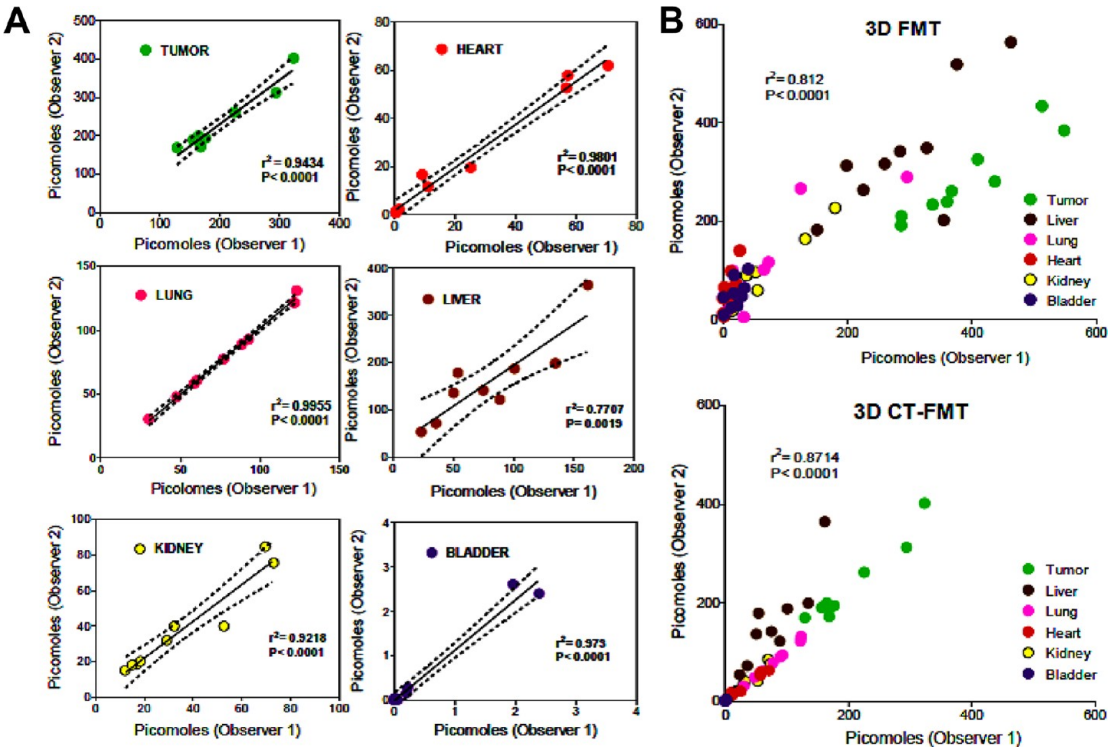

Figure 4. Robustness of CT-based organ segmentation and CT-FMT fusion. (A) FMT-based fluorescence signals obtained upon organ presegmentation performed by two independent observers were compared and correlated (using linear regression analysis) for tumor, heart, lung, liver, kidney, and bladder, confirming the robustness of this procedure. (B) Comparison and correlation of all individual organ accumulation values obtained upon 3D FMT and 3D CT-FMT, exemplifying the lower interindividual variability of CT-FMT as compared to standard FMT.

Robustness of CT-Based Organ Segmentation. The robustness of the 3D μCT-based organ segmentation protocol, and of fusing the μCT data sets with the data sets obtained using 3D FMT, was validated by comparing and correlating the results obtained by two different observers. To this end, two blinded observers independently determined the μCT-based volumes for tumor, liver, kidney, bladder, lung, and heart for all nine mice (at one time point after i.v. administration, *i.e.*, at 72 h p.i.), they independently fused these data sets with the 3D FMT data sets obtained on the biodistribution of pHPMA-Dy750 at this time point, and their results were compared. As exemplified by Figure 4A, these analyses showed that the proposed protocol was highly reproducible, with both observers obtaining very comparable results with regard to probe accumulation in tumor, heart, lung, kidney, and bladder. Correlation coefficients (r^2) were always well above 0.9, and p values were always <0.0001. Only for liver, which is relatively difficult to properly segment in 3D using non-contrast-enhanced μCT, the correlation coefficient was found to be lower ($r^2 = 0.77$), but even in this case, a highly significant p value was obtained ($p = 0.002$), exemplifying the validity of this segmentation and probe accumulation protocol. Taking the relatively uninformative 3D FMT images in Figure 2B and the much more accurate 3D CT-FMT images in Figure 3A into account, it is obvious that accurate organ segmentation and quantitative probe accumulation analyses are much more feasible when using hybrid CT-FMT as compared to only FMT. This is quantitatively demonstrated in Figure 4B, in which the accumulation of pHPMA-Dy750 in tumors and in several different healthy organs was analyzed by two different observers using both FMT and CT-FMT, and in which the results were correlated. For 3D FMT, a correlation coefficient of 0.81 was obtained, as compared to 0.87 for CT-FMT. When excluding the liver, which is relatively difficult to segment using non-contrast-enhanced μCT, a significantly higher ($p < 0.001$) correlation coefficient was found for CT-FMT ($r^2 = 0.99$) compared to 3D FMT ($r^2 = 0.87$).

Monitoring the Tumor Accumulation of pHPMA-Dy750 Using CT-FMT. Upon having demonstrated the advantage of 3D CT-FMT over standard 3D FMT for monitoring the biodistribution of NIRF-labeled nanomedicine formulations, we sought to validate the usefulness of 3D CT-FMT for quantifying the tumor accumulation of pHPMA-Dy750. To this end, as shown in Figure 5, EPR-mediated passive drug targeting to tumors was compared upon 2D FRI, 3D FMT, and 3D CT-FMT analysis. Using 2D FRI, continuously increasing levels in the tumors were observed, confirming strong tumor accumulation, but not providing quantitative information on the overall efficiency of tumor targeting (values in counts per energy; see top panel in Figure 5B). Using 3D FMT, in line with

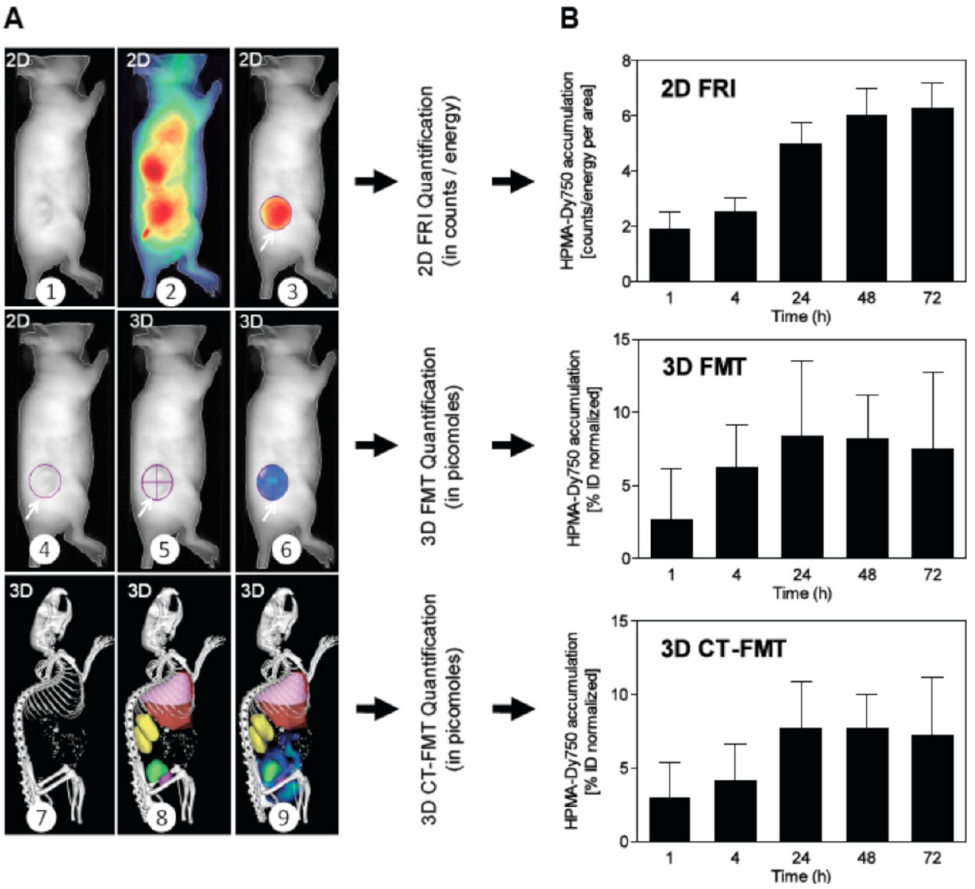

Figure 5. Optical imaging of the tumor accumulation of pHPMA-Dy750. (A) Schematic depiction of the methodology employed for (semi-) quantitative 2D FRI, 3D FMT, and 3D CT-FMT tumor accumulation analyses. Panel 1 shows a standard white-light image of a pHPMA-Dy750-treated mouse and the corresponding FRI image (2). On the basis of panel 1, a 2D ROI was placed over the tumor region, and the FRI signal (in counts/energy) corresponding to this 2D ROI was determined. Next, in the same image, the 2D FRI signal was temporarily turned off, and on the basis of the 2D ROI (circle in 4), a 3D ROI was carefully superimposed over the tumor region (crossed circle in 5), enabling 3D FMT analysis of target site accumulation in picomoles (6). As outlined in Figure 3, the tumor was then manually segmented on the basis of non-contrast-enhanced CT imaging (7 and 8) and fused with the FMT signals generated as part of panel 6, to accurately quantify the tumor accumulation of pHPMA-Dy750 using hybrid CT-FMT (9). (B) Quantification of the tumor accumulation of pHPMA-Dy750 in CT26 colon carcinoma-bearing mice using 2D FRI, 3D FMT, and 3D CT-FMT. For 3D FMT and 3D CT-FMT, values are normalized to average tumor volumes at the respective time points. Values represent average ± standard deviation (n = 9).

previous analyses using radiolabeled polymeric nanomedicines,[12,34,36−39] levels seemed to plateau after 24 h p.i. (middle panel in Figure 5B). Analogously, also upon 3D CT-FMT, concentrations in tumors seemed to plateau after 24 h (bottom panel in Figure 5B). As compared to 3D FMT, the standard deviations of the amounts of pHPMA-Dy750 accumulating in tumors as analyzed using 3D CT-FMT were found to be somewhat smaller, confirming the robustness and the enhanced accuracy of this methodology.

An added advantage of CT-FMT as compared to standard FMT relates to the fact that, using the former, the 3D distribution of nanomedicine formulations within tumors and/or their penetration into the tumor core can be evaluated in much more detail. This is exemplarily depicted in Figure 6, showing that when subdividing an ~8 mm sized CT26 tumor into 15 different 0.5 mm segments, and then stepwise analyzing the accumulation of pHPMA-Dy750 in this tumor using OI, 3D CT-FMT enables the acquisition of noninvasive imaging information on probe accumulation in the periphery (*i.e.*, segments 1−6 and 11−15) *versus* the core (*i.e.*, segments 7−10) of this tumor, hinting toward a stronger accumulation of the polymer in the outer *versus* the inner parts. This is in line with the literature[4,10−12] and can be explained either by a better perfusion of the periphery *versus* the core of subcutaneous tumors or by necrosis in the center of the tumor. Irrespective of the biological and/or pathophysiological reason for this difference, these findings exemplify that 3D CT-FMT is more suitable than standard 3D FMT for noninvasively visualizing and quantifying the tumor accumulation and the intratumoral distribution of NIRF-labeled nanomedicines using OI.

Noninvasive Optical Imaging of Nanomedicine Biodistribution Using 3D CT-FMT. Both 2D FRI (because of limited penetration depth) and 3D FMT (because of limited anatomical information and spatial resolution) do not allow for an accurate noninvasive assessment of

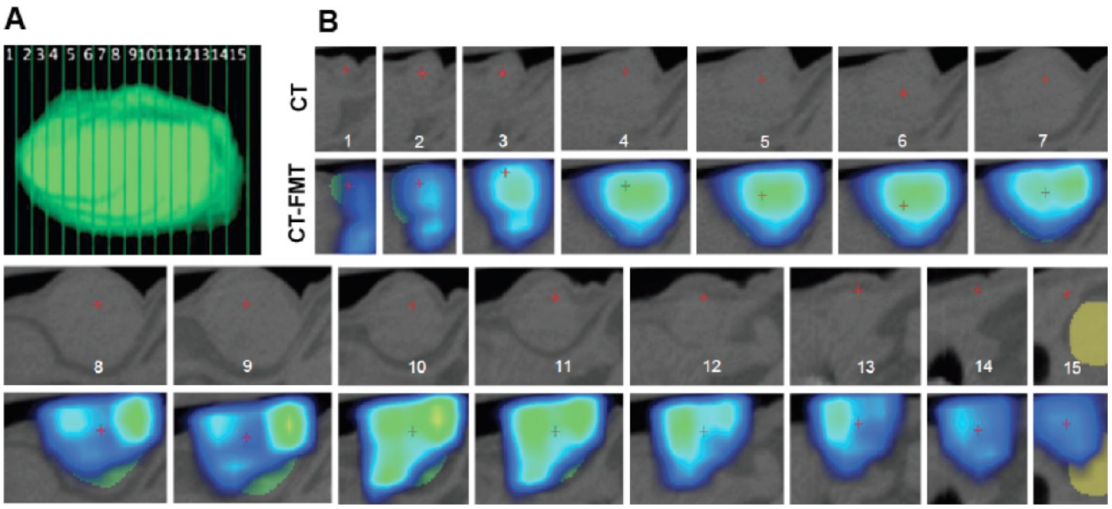

Figure 6. Monitoring the intratumoral distribution of pHPMA-Dy750 using 3D CT-FMT. (A,B) Accumulation of pHPMA-Dy750 in 15 consecutive 0.5 mm wide cross-sectional CT slices (A) was evaluated using hybrid 3D CT-FMT, exemplifying inhomogeneous intratumoral probe distribution, with lower levels in the core *vs* the periphery (B).

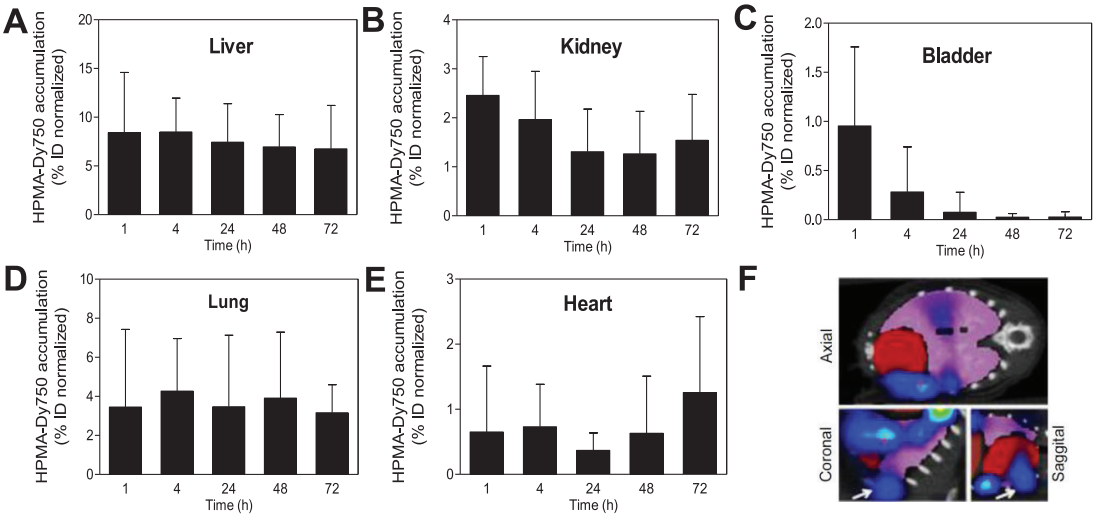

Figure 7. Noninvasive quantification of the accumulation of pHPMA-Dy750 in healthy organs using 3D CT-FMT. (A–E) Accumulation of pHPMA-Dy750 in liver (A), kidney (B), bladder (C), lung (D), and heart (E) at several different time points after i.v. injection. The percentages of injected dose were normalized to the respective organ volumes. Values represent average ± standard deviation (n = 9). (F) Representative image of pHPMA-Dy750 localization in heart and lung at 1 h p.i., exemplifying that, due the presence of large amounts of blood in the heart and/or of air in the lung, the fluorescence signal that should be allocated to the heart at this early time point (cf. Figure 2A) is seriously distorted, leading to an inappropriate representation and quantification (cf. panel E) of the long-circulating properties of this polymeric nanomedicine formulation.

nanomedicine accumulation in healthy organs and tissues. To overcome this shortcoming, as described above, we have here for the first time set out to develop a μCT-based organ segmentation protocol which enables the fusion of functional 3D FMT information on the biodistribution of NIRF-labeled nanocarriers, with 3D anatomical information on organ localization. Figure 3 schematically depicts the procedure employed for combining μCT-based organ segmentation with FMT-based biodistribution studies, and Figure 7 shows the results obtained using this procedure. As can be clearly seen, 3D CT-FMT realistically depicted probe accumulation in liver, kidney, and bladder. Both absolute (%ID) and relative (organ-to-organ) values were relatively well in line with those reported in the literature for radiolabeled polymeric nanomedicines.[12,34,36–39] Furthermore, as for tumors (Figure 5), also the time-dependent trends in liver, kidney, and bladder accumulation were in line with previous studies, with liver remaining relatively constant over time and kidney and bladder decreasing.[12,34,36] Also for lung, levels of accumulation and time-dependent trends were also quite comparable to studies performed using radiolabeled polymers. For heart, on the other hand, the results were very different from those reported previously, as the overall levels were much lower than what would be expected for

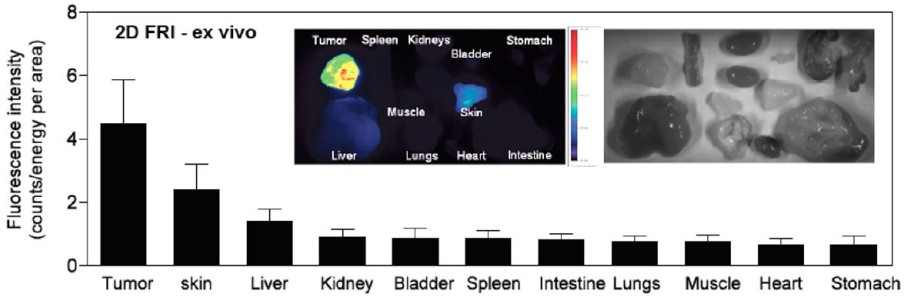

Figure 8. ***Ex vivo*** **analysis of pHPMA-Dy750 tumor and organ accumulation. Two-dimensional FRI-based quantification of pHPMA-Dy750 accumulation in tumors and healthy organs at 72 h p.i. Values are expressed in counts/energy per area (*i.e.*, corrected for surface area) and represent average ± standard deviation (n = 9). Inset: Visual depiction of 2D FRI and bright field images, showing probe accumulation in excised tumors and healthy organs at 72 h p.i.**

long-circulating nanomedicines, and as concentration tended to increase, rather than decrease, over time. This, however, can be explained by the anatomical location of the heart, as it is surrounded by the lungs, and as the air−tissue interface distorts the localization and quantification of fluorescent signals. Moreover, also the strong absorption of blood likely contributes substantially to the inaccuracies in accumulation patterns in the heart. In spite of these shortcomings, it seems to be justified on the basis of these initial proof-of-principle findings that combining anatomical μCT with functional FMT substantially facilitates the noninvasive assessment of nanomedicine biodistribution.

Ex Vivo **Validation of Nanomedicine Biodistribution Using 2D FRI.** Finally, we evaluated the organ distribution of pHPMA-Dy750 using *ex vivo* 2D FRI. This is because *ex vivo* organ analyses are routinely performed in experiments in which NIRF-labeled nanocarriers are being evaluated, to complement the results obtained noninvasively on tumor targeting potential and to semiquantitatively compare tumor *versus* healthy organ accumulation at at least one time point (*i.e.*, at the end of the experiment). To this end, after completing the 3D CT-FMT scans at 72 h p.i., tumors and healthy organs (*i.e.*, liver, spleen, lung, kidney, heart, bladder, muscle, intestine, skin, and stomach) were excised and scanned *ex vivo* using 2D FRI. As shown in Figure 8A, when visually interpreting the results, *ex vivo* FRI indicated very strong probe accumulation in tumors and less localization in healthy organs. When quantifying the results (by drawing regions-of-interest, and by correcting probe accumulation to surface area), however, concentrations appeared to be somewhat more balanced and realistic (Figure 8B). Though it is impossible to directly compare these FRI results (which are strongly surface-dominated and at best semiquantitative) to those obtained using CT-FMT, it is obvious that the tendencies are comparable, with very strong EPR-mediated tumor targeting observable in both cases, and with, besides in tumor, also significant accumulation in the liver. The clear advantage of 3D CT-FMT over 2D FRI, however, is that it can be employed to noninvasively assess probe accumulation in tumors and in healthy organs over time (cf. Figures 3, 5, 6, and 7), which is impossible using 2D FRI (cf. Figures 2 and 8). Therefore, although it is obvious that there are still several important hurdles to be overcome before OI can be widely adopted for quantitative biodistribution monitoring (related, for example, to problems caused by the air−tissue interface and/or by strong light absorption by blood in highly perfused organs, such as the heart; see Figure 7E,F), it seems to be justified to conclude that combining anatomical μCT with functional FMT holds significant potential for noninvasively assessing the biodistribution of nanomedicine formulations.

CONCLUSIONS

In the past 5 to 10 years, the use of *in vivo* optical imaging (OI) techniques has increased exponentially. Besides for molecular imaging purposes, OI has also been more and more used for monitoring the biodistribution and target site accumulation of nanomedicine formulations. To overcome some of the shortcomings associated with OI of nanomedicine biodistribution, in particular, those related to the lack of anatomical information, we developed a hybrid CT-FMT-based imaging protocol to enable more meaningful and more quantitative *in vivo* analyses. Long-circulating fluorophore-labeled polymeric drug carriers were used to validate the usefulness of this protocol, resulting in levels of tumor and healthy organ accumulation comparable to those reported in the literature. Consequently, these initial proof-of-principle experiments convincingly show that combining anatomical μCT with molecular FMT facilitates the noninvasive assessment of nanomedicine biodistribution.

METHODS

Materials. 1-Aminopropan-2-ol, methacryloyl chloride, dichloromethane (DCM), sodium carbonate, glycylglycine (GG), 4,5-dihydrothiazole-2-thiol (TT), 2,2′-azobis(isobutyronitrile) (AIBN), 6-aminohexanoic acid (AH), *N*,*N*-dimethylformamide (DMF), *N*,*N*′-dicyclohexylcarbodiimide (DCC), dimethylsulfoxide

(DMSO), *N*,*N*-diisopropylethylamine (DIPEA), diethylether, and methanol were purchased from Fluka. The near-infrared fluorescent dye Dy750-NH_2 was purchased from Dyomics GmbH, Germany.

Synthesis and Characterization of pHPMA-Dy750. *N*-(2-Hydroxypropyl)methacrylamide (HPMA) was synthesized by reaction of methacryloyl chloride with 1-aminopropan-2-ol in DCM using sodium carbonate. *N*-Methacryloyl glycylglycine (Ma-GG-OH) was prepared by Schotten–Baumann acylation of glycylglycine with methacryloyl chloride in aqueous alkaline medium. 3-(*N*-Methacryloyl glycylglycyl)thiazolidine-2-thione (Ma-GG-TT) was prepared by the reaction of Ma-GG-OH with 4,5-dihydrothiazole-2-thiol in DMF in the presence of DCC. The multivalent random copolymer precursor poly(HPMA-*co*-Ma-GG-TT) was prepared by solution radical copolymerization of HPMA (85 mol %) and Ma-GG-TT (15 mol %) in DMSO at 50 °C for 6 h. The concentration of monomers in the copolymerization mixture was 12.5% w/w, and that of the initiator AIBN was 1.5% w/w. The molecular weight of polymer precursor was 65 kDa, and its polydispersity index (M_W/M_N) was 1.7. The polymer precursor poly(HPMA-*co*-Ma-GG-TT) (39 mg, 0.78 mmol TT group per gram of polymer) was dissolved in methanol (0.6 mL). Dy750-NH_2 (1 mg; 1.26 μmol) and DIPEA (0.43 μL, 2.52 μmol) were added. After a 0.5 h reaction with the fluorescent dye, the polymer was aminolyzed with 1-aminopropan-2-ol (5 μL). Fifteen minutes later, the aminolyzed copolymer was isolated by precipitation with diethylether, followed by centrifugation. The precipitate was dried under vacuum. Then, the dry copolymer was dissolved in water, purified by gel filtration on Sephadex G-25 in water (PD 10 column; Pharmacia), and freeze-dried, yielding 31 mg (80%) of poly(HPMA-*co*-Ma-GG-Dy750-*co*-Ma-GG-AP) (pHPMA-Dy750). The content of fluorescent dye was 2.5 wt %. The molecular weight and the polydispersity index of pHPMA-Dy750 were 67 kDa and 1.7, respectively.[40–42]

Animal Experiments. All animal experiments were approved by local and/or national regulatory authorities and ethical committees regarding animal welfare. CD-1 nude mice (n = 9) weighing 25–30 g were fed chlorophyll-free food pellets and water *ad libitum*. Mice were housed in ventilated cages and clinically controlled rooms and atmosphere. CT26 colon carcinoma tumor cells (ATCC) were cultured in Dulbecco's modified Eagle's medium (DMEM; Gibco, Invitrogen, Germany), supplemented with 10% fetal bovine serum (FBS) (Invitrogen, Germany) and 1% pen/strep (10 000 U/mL penicillin; 10 000 μg/mL streptomycin, Invitrogen, Germany) at 37 °C and 5% CO_2, in a humidified atmosphere. Mice were inoculated with CT26 tumor cells (1×10^6 cells/100 μL) subcutaneously into the right flank. Before performing the imaging experiments, the growth of CT26 tumor xenografts was monitored constantly for 10–14 days, until a size of 6–8 mm was reached.

Probe Calibration and Administration. pHPMA-Dy750 was solubilized in PBS and calibrated using standard FMT protocols. Based on calibration, a scaling factor was generated and validated (to confirm compliance with the theoretical yield of fluorescence intensity). pHPMA-Dy750 was injected intravenously *via* the tail vein, at a dose of 2.5 nmol (Dy750 equivalent), and its biodistribution was monitored according to the protocols listed below. No toxicity was observed after the administration of the probe and throughout the study.

Imaging Protocols. *MicroCT.* CD-1 nude mice bearing CT26 colon carcinoma xenografts were first subjected to high-resolution dual-energy microCT imaging (Tomoscope DUO; CT Imaging, Erlangen, Germany). Animals with tumors of an average size of ~8 mm were anaesthetized using a 2.5% mixture of isoflurane/O_2. Mice were then placed onto a multimodal imaging cassette (CT-imaging, Erlangen, Germany), and depths were adjusted with the tumor rightly projecting upward and placed toward the center of the imaging cassette. The following scanning protocol was employed: both tubes were run at 65 kV and a current of 0.5 mA; each flat panel detector acquired 720 projections containing 1032×1012 pixels in a full gantry rotation with duration of 90 s; all images were reconstructed with an isotropic voxel size of 35 μm, using a modified Feldkamp algorithm with a smooth kernel.

FMT. Directly after the microCT scan, without changing the orientation and position of the animal in the imaging cassette, mice were placed into the internal FMT docking station (FMT2500; PerkinElmer), under controlled anesthesia and temperature. Parameters such as excitation wavelength channel, imaging agent, *etc*. were preset by the FMT2500, based on the calibration details obtained for pHPMA-Dy750. The depth of the imaging cassette was automatically set by the FMT instrument. Initially, whole body images of the mice were captured using FRI. On the basis of these images, the region of interest was set and 3D scans were performed. The spatial density of the scanning mode was set to "medium" (*i.e.*, the 3 mm default setting). Animals were prescanned prior to injection to rule out autofluorescence. Three-dimensional imaging was carried out at various time points (*i.e.*, at 0.25, 0.5, 1, 4, 24, 48, and 72 h). On the basis of the FMT signals obtained, the interuser variability in assessing organ accumulation (in picomoles) was validated.

MicroCT-FMT Fusion. The obtained 3D μCT and 3D FMT data sets were fused by rigid transformation using fiducial markers in the mouse cartridge. On the basis of the μCT data, organs such as liver, kidney, lung, heart, urinary bladder, and tumor were manually segmented using an Imalytics Research Workstation (Philips Technologie GmbH Innovative Technologies, Aachen, Germany). High-resolution μCT imaging takes approximately 5 min per mouse and another 5 min for each corresponding FMT scan. In total, hybrid CT-FMT takes 10–15 min, depending on the number of FMT scans performed. The robustness of the μCT-based organ segmentation protocol for probe quantification was validated by comparing and correlating the results obtained by two independent observers. Finally, FMT signals were overlaid onto organ-segmented μCT images, and the amounts of pHPMA-Dy750 in these organs were quantified. The percentage injected dose (%ID) was calculated based on the quantification values obtained for each segmented organ.

Ex Vivo Organ Analysis. Seventy two hours after the administration of pHPMA-Dy750, animals were sacrificed, and tumors and several different healthy organs (*i.e.*, liver, kidney, spleen, heart, lung, urinary bladder, intestine, skin, and stomach) were removed, weighed, and analyzed by 2D FRI. In addition, tumors from all nine mice were adjacently placed, *ex vivo* FRI scans were performed, and probe accumulation was compared.

Statistical Analysis. Results are presented as average ± standard deviation. Statistical analyses were performed using GraphPad Prism 5.01, using the two-tailed student's t test and determination of correlation coefficients. In both cases, a p value <0.05 was considered to represent statistical significance. To compare correlation coefficients in user-reproducibility, the fisher z test was used.

Conflict of Interest: The authors declare no competing financial interest.

Acknowledgment. The authors gratefully acknowledge technical support by Diana Moeckel, and financial support by the German Federal State of North Rhine Westphalia (NRW; HighTech.NRW/EU-Ziel 2-Programm (EFRE); ForSaTum), the European Union (European Regional Development Fund - Investing In Your Future; COST-Action TD1004; and ERC-StG309495-NeoNaNo), the DFG (LA2937/1-1) and the GACR (P-301/11/0325).

REFERENCES AND NOTES

1. Davis, M. E.; Chen, Z.; Shin, D. M. Nanoparticle Therapeutics: An Emerging Treatment Modality for Cancer. *Nat. Rev. Drug Discovery* **2008**, *7*, 771–782.
2. Lammers, T.; Hennink, W. E.; Storm, G. Tumour-Targeted Nanomedicines: Principles and Rractice. *Br. J. Cancer* **2008**, *99*, 392–397.
3. Farokhzad, O. C.; Langer, R. Impact of Nanotechnology on Drug Delivery. *ACS Nano* **2009**, *3*, 16–20.
4. Jain, R. K.; Stylianopoulos, T. Delivering Nanomedicine to Solid Tumors. *Nat. Rev. Clin. Oncol.* **2010**, *7*, 653.
5. Duncan, R.; Gaspar, R. Nanomedicine(s) under the Microscope. *Mol. Pharmaceutics* **2011**, *8*, 2101–2141.
6. Matsumura, Y.; Maeda, H. A New Concept for Macromolecular Therapeutics in Cancer Chemotherapy: Mechanism

of Tumoritropic Accumulation of Proteins and the Antitumor Agent Smancs. *Cancer Res.* **1986**, *46*, 6387–6392.
7. Maeda, H.; Wu, J.; Sawa, T.; Matsumura, Y.; Hori, K. Tumor Vascular Permeability and the EPR Effect in Macromolecular Therapeutics: A Review. *J. Controlled Release* **2000**, *65*, 271–284.
8. Maeda, H. The Enhanced Permeability and Retention (EPR) Effect in Tumor Vasculature: the Key Role of Tumor-Selective Macromolecular Drug Targeting. *Adv. Enzyme Regul.* **2001**, *41*, 189–207.
9. Lammers, T.; Kiessling, F.; Hennink, W. E.; Storm, G. Nanotheranostics and Image-Guided Drug Delivery: Current Concepts and Future Directions. *Mol. Pharmaceutics* **2010**, *7*, 1899–1912.
10. Lammers, T.; Subr, V.; Ulbrich, K.; Hennink, W. E.; Storm, G.; Kiessling, F. Polymeric Nanomedicines for Image-Guided Drug Delivery and Tumor-Targeted Combination Therapy. *Nano Today* **2010**, *5*, 197–212.
11. Mulder, W. J. M.; Strijkers, G. J.; van Tilborg, G. A. F.; Cormode, D. P.; Fayad, Z. A.; Nicolay, K. Nanoparticulate Assemblies of Amphiphiles and Diagnostically Active Materials for Multimodality Imaging. *Acc. Chem. Res.* **2009**, *42*, 904–914.
12. Lammers, T.; Subr, V.; Peschke, P.; Kuhnlein, R.; Hennink, W. E.; Ulbrich, K.; Kiessling, F.; Heilmann, M.; Debus, J.; Huber, P. E.; *et al.* Image-Guided and Passively Tumour-Targeted Polymeric Nanomedicines for Radiochemotherapy. *Br. J. Cancer* **2008**, *99*, 900–910.
13. Lammers, T.; Subr, V.; Ulbrich, V.; Peschke, P.; Huber, P. E.; Hennink, W. E.; Storm, G. Simultaneous Delivery of Doxorubicin and Gemcitabine to Tumors *in Vivo* Using Prototypic Polymeric Drug Carriers. *Biomaterials* **2009**, *30*, 3466–3475.
14. Lammers, T.; Aime, S.; Hennink, W. E.; Storm, G.; Kiessling, F. Theranostic Nanomedicine. *Acc. Chem. Res.* **2011**, *44*, 1029–1038.
15. Kunjachan, S.; Jayapaul, J.; Mertens, M. E.; Storm, G.; Kiessling, F.; Lammers, T. Theranostic Systems and Strategies for Monitoring Nanomedicine-Mediated Drug Targeting. *Curr. Pharm. Biotechnol.* **2012**, *13*, 609–622.
16. Licha, K.; Olbrich, C. Optical Imaging in Drug Discovery and Diagnostic Applications. *Adv. Drug Delivery Rev.* **2005**, *57*, 1087–1108.
17. Veiseh, O.; Sun, C.; Gunn, J.; Kohler, N.; Gabikian, P.; Lee, D.; Bhattarai, N.; Ellenbogen, R.; Sze, R.; Hallahan, A.; *et al.* Optical and MRI Multifunctional Nanoprobe for Targeting Gliomas. *Nano Lett.* **2005**, *5*, 1003–1008.
18. Roy, I.; Ohulchanskyy, T. Y.; Bharali, D. J.; Pudavar, H. E.; Mistretta, R. A.; Kaur, N.; Prasad, P. N. Optical Tracking of Organically Modified Silica Nanoparticles as DNA Carriers: A Nonviral Nanomedicine Approach for Gene Delivery. *Proc. Natl. Acad. Sci. U.S.A.* **2005**, *102*, 279–284.
19. Liong, M.; Lu, J.; Kovochich, M.; Xia, T.; Ruehm, S. G.; Nel, A. E.; Tamanoi, F.; Zink, J. I. Multifunctional Inorganic Nanoparticles for Imaging, Targeting, and Drug Delivery. *ACS Nano* **2008**, *2*, 889–896.
20. Janib, S. M.; Moses, A. S.; MacKay, J. A. Imaging and Drug Delivery Using Theranostic Nanoparticles. *Adv. Drug Delivery Rev.* **2010**, *62*, 1052–1063.
21. Hwang, H. Y.; Kim, I. S.; Kwon, I. C.; Kim, Y. H. Tumor Targetability and Antitumor Effect of Docetaxel-Loaded Hydrophobically Modified Glycol Chitosan Nanoparticles. *J. Controlled Release* **2008**, *128*, 23–31.
22. Lee, S.; Ryu, J. H.; Park, K.; Lee, A.; Lee, S. Y.; Youn, I. C.; Ahn, C. H.; Yoon, S. M.; Myung, S. J.; Moon, D. H.; *et al.* Polymeric Nanoparticle-Based Activatable Near-Infrared Nanosensor for Protease Determination *in Vivo*. *Nano Lett.* **2009**, *9*, 4412–4416.
23. Kim, K.; Kim, J. H.; Park, H.; Kim, Y. S.; Park, K.; Nam, H.; Lee, S.; Park, J. H.; Park, R. W.; Kim, I. S.; *et al.* Tumor-Homing Multifunctional Nanoparticles for Cancer Theragnosis: Simultaneous Diagnosis, Drug Delivery, and Therapeutic Monitoring. *J. Controlled Release* **2010**, *146*, 219–227.
24. Gao, J.; Chen, K.; Luong, R.; Bouley, D. M.; Mao, H.; Qiao, T.; Gambhir, S. S.; Cheng, Z. A Novel Clinically Translatable Fluorescent Nanoparticle for Targeted Molecular Imaging of Tumors in Living Subjects. *Nano Lett.* **2012**, *12*, 281–286.
25. Poon, Z.; Lee, J. B.; Morton, S. W.; Hammond, P. T. Controlling *In Vivo* Stability and Biodistribution in Electrostatically Assembled Nanoparticles for Systemic Delivery. *Nano Lett.* **2011**, *11*, 2096–2103.
26. Ntziachristos, V.; Ripoll, J.; Wang, L. V.; Weissleder, R. Looking and Listening to Light: The Evolution of Whole-Body Photonic Imaging. *Nat. Biotechnol.* **2005**, *23*, 313–320.
27. Ntziachristos, V.; Tung, C. H.; Bremer, C.; Weissleder, R. Fluorescence Molecular Tomography Resolves Protease Activity *in Vivo*. *Nat. Med.* **2002**, *8*, 757.
28. Graves, E. E.; Ripoll, J.; Weissleder, R.; Ntziachristos, V. A Submillimeter Resolution Fluorescence Molecular Imaging System for Small Animal Imaging. *Med. Phys.* **2003**, *30*, 901–911.
29. Ntziachristos, V.; Weissleder, R. Experimental Three-Dimensional Fluorescence Reconstruction of Diffuse Media by Use of a Normalized Born Approximation. *Opt. Lett.* **2001**, *26*, 893–895.
30. Ntziachristos, V. Fluorescence Molecular Imaging. *Annu. Rev. Biomed. Eng.* **2006**, *8*, 1–33.
31. Nahrendorf, M.; Keliher, E.; Marinelli, B.; Waterman, P.; Feruglio, P. F.; Fexon, L.; Pivovarov, M.; Swirski, F. K.; Pittet, M. J.; Vinegoni, C.; *et al.* Hybrid PET-Optical Imaging Using Targeted Probes. *Proc. Natl. Acad. Sci. U.S.A.* **2010**, *107*, 7910–7915.
32. Schulz, R. B.; Ale, A.; Sarantopoulos, A.; Freyer, M.; Soehngen, E.; Zientkowska, M.; Ntziachristos, V. Hybrid System for Simultaneous Fluorescence and X-ray Computed Tomography. *IEEE Trans. Med. Imaging* **2010**, *29*, 465–473.
33. Panizzi, P.; Nahrendorf, M.; Figueiredo, J. L.; Panizzi, J.; Marinelli, B.; Iwamoto, Y.; Keliher, E.; Maddur, A. A.; Waterman, P.; Kroh, H. K.; *et al. In Vivo* Detection of *Staphylococcus aureus* Endocarditis by Targeting Pathogen-Specific Prothrombin Activation. *Nat. Med.* **2011**, *17*, 1142–1146.
34. Lammers, T.; Kuhnlein, R.; Kissel, M.; Subr, V.; Etrych, T.; Pola, R.; Pechar, M.; Ulbrich, K.; Storm, G.; Huber, P.; *et al.* Effect of Physicochemical Modification on the Biodistribution and Tumor Accumulation of HPMA Copolymers. *J. Controlled Release* **2005**, *110*, 103–118.
35. Lammers, T.; Ulbrich, K. HPMA Copolymers: 30 Years of Advances. *Adv. Drug Delivery Rev.* **2010**, *62*, 119–121.
36. Lammers, T.; Peschke, P.; Kuhnlein, R.; Subr, V.; Ulbrich, K.; Debus, J. A.; Huber, P.; Hennink, W.; Storm, G. Effect of Radiotherapy and Hyperthermia on the Tumor Accumulation of HPMA Copolymer-Based Drug Delivery Systems. *J. Controlled Release* **2007**, *117*, 333–341.
37. Seymour, L. W.; Miyamoto, Y.; Maeda, H.; Brereton, M.; Strohalm, J.; Ulbrich, K.; Duncan, R. Influence of Molecular Weight on Passive Tumour Accumulation of a Soluble Macromolecular Drug Carrier. *Eur. J. Cancer* **1995**, *31*, 766–770.
38. Pimm, M. V.; Perkins, A. C.; Duncan, R.; Ulbrich, K. Targeting of *N*-(2-Hydroxypropyl)methacrylamide Copolymer-Doxorubicin Conjugate to the Hepatocyte Galactose-Receptor in Mice: Visualisation and Quantification by Gamma Scintigraphy as a Basis for Clinical Targeting Studies. *J. Drug Target* **1993**, *1*, 125–131.
39. Shiah, J. G.; Dvorak, M.; Kopeckova, P.; Sun, Y.; Peterson, C. M.; Kopecek, J. Biodistribution and Antitumour Efficacy of Long-Circulating *N*-(2-Hydroxypropyl)methacrylamide Copolymer Doxorubicin Conjugates in Nude Mice. *Eur. J. Cancer* **2001**, *37*, 131–139.
40. Ulbrich, K.; Subr, V.; Strohalm, J.; Plocova, D.; Jelinkova, M.; Rihova, B. Polymeric Drugs Based on Conjugates of Synthetic and Natural Macromolecules. I. Synthesis and Physico-Chemical Characterization. *J. Controlled Release* **2000**, *64*, 63–79.
41. Etrych, T. A.; Mrkvan, T. A.; Chytil, P.; Konak, C.; Rihova, B.; Ulbrich, K. *N*-(2-Hydroxypropyl)methacrylamide-Based Polymer Conjugates with pH-Controlled Activation of

Doxorubicin. I. New Synthesis, Physicochemical Characterization and Preliminary Etiological Evaluation. *J. Appl. Polym. Sci.* **2008**, *109*, 3050–3061.
42. Etrych, T. A.; Mrkvan, T. A.; Rihova, B.; Ulbrich, K. Star-Shaped Immunoglobulin-Containing HPMA-Based Conjugates with Doxorubicin for Cancer Therapy. *J. Controlled Release* **2007**, *122*, 31–38.